Hexapod Hall scanner for high-resolution large area magnetic imaging

G. K. Perkins, M. Kustov, E. Lovell, M. V. Pettifer, and L. F. Cohen

Citation: Review of Scientific Instruments **89**, 065111 (2018); doi: 10.1063/1.5020024
View online: https://doi.org/10.1063/1.5020024
View Table of Contents: http://aip.scitation.org/toc/rsi/89/6
Published by the American Institute of Physics

Hexapod Hall scanner for high-resolution large area magnetic imaging

G. K. Perkins, M. Kustov, E. Lovell, M. V. Pettifer, and L. F. Cohen
Blackett Laboratory, Department of Physics, Imperial College, Prince Consort Road, South Kensington, London SW7 2AZ, United Kingdom

(Received 19 December 2017; accepted 1 June 2018; published online 21 June 2018)

We demonstrate a six-axis scanning imaging apparatus using piezo bending actuators with a large scan range. The six axes of motion of the bending actuators together with the coupling mechanism to the translation stage allow complete control of the sensor position and orientation over the scanning surface, which is ideal for the use of planar sensors such as Hall devices. In particular, the design allows for *in situ* correction of the probe tilt angle so that the sensor distance to sample surface can be minimized. We investigate the impact of this alignment on the quality of the measured data using an InSb Hall sensor and a magnetic sample. We also demonstrate a synchronous commutation setup that can greatly enhance the magnetic image by reducing the Hall signal offset. *Published by AIP Publishing.* https://doi.org/10.1063/1.5020024

I. INTRODUCTION

Scanning Hall probe microscopy is a powerful magnetic imaging technique that offers a unique combination of large scan range and submicron spatial resolution in combination with high sensitivity up to a high applied magnetic field.[1–4] The non-invasive nature of the imaging process and the relative simplicity of the reconstruction procedure of the magnetic field distribution from a measured Hall voltage facilitate the use of the technique for a variety of applications. Some of these applications include the study of superconductors,[5–7] magnetic flux micro-sources,[8–10] magnetic domain structure in films,[11] and the magnetic phase transition in magneto-caloric materials.[12–16]

The scan range of a Hall probe system depends on the type of scanning system employed. Motorized implementations typically have a range of $\sim 10^{-2}$ m, whereas conventional piezo scanners [e.g., lead zirconium titanate (PZT) piezoelectric transducer tubes] cover $\sim 10^{-4}$ m and PZT bending actuator based scanners up to 10^{-3} m. It is the latter that we implement in our design as they are most suitable for the resolution of our Hall devices and work well in cryogenic/high magnetic field environments. While motorized scanning stages are normally restricted to room temperature and low magnetic field (unless more complex coupling to the sensor is implemented[17]), piezo systems are largely unaffected by magnetic field and work well at cryogenic temperatures, albeit with a reduced spatial range.

For Hall probe imaging, the effective spatial resolution or pixel size is determined by several limiting factors including the active area of the Hall sensor, the distance between the active area and the sample surface, and the minimum incremental step size of the scanner. In practice, the first two usually prove to be limiting[7] although mechanical scanners often exhibit significant backlash (greater than the incremental step size) and care must be taken to mitigate its effects.

The size of the probe active area is determined by the fabrication process and can be as small as 200 nm[18] for semiconductor devices although only 1 μm devices and above are readily available commercially. It should also be noted that for a given material type, sensitivity is roughly proportional to sensor dimensions, so it may not always be desirable to minimize the sensor size. For example, very small Hall probes (~100 nm) have been fabricated using bismuth films but with greatly reduced sensitivity.[19,20] In principle, graphene sensors could be extremely promising.[21–24]

The importance of keeping the sensor-sample distance as small as possible for the lateral resolution is discussed by Lima and co-authors in Ref. 25. The sensor-sample distance depends the ability to keep the scanned probe in contact or in controlled near-surface proximity to the investigated sample and also the alignment between the sensor and the sample (i.e., the tilt of the sensor with respect to the sample surface). The hexapod scanner described here allows optimization with regard to the latter point, setting it aside from the usual scanner designs. Its design and functionality are described below.

II. INSTRUMENT DESIGN

A. Mechanical design of the scanner head

Piezo bender-based scanners are used in a wide range of modalities[26] such as high-speed AFM[27] and optical micro-scanning mirror control[28] and bridge the capabilities of motorized and shear-actuator based scanners. In the present case, the hexapod uses six piezo bending actuators (PBAs) to move a translation stage (TS) in six axes (the three Cartesian axes x, y, and z and three rotations about these axes θ_x, θ_y, and θ_z, respectively). The use of bending actuators (as opposed to the tube actuators used in many piezo scanners) offers two main advantages.

- Increased spatial range, currently around 1 mm, and typically an order of magnitude larger than conventional piezo scanners.
- Low voltage operation. Multilayer bending actuators typically operate in the range 0-60 V rather than 0-1000 V employed with conventional piezo scanners.

The unique aspect of this hexapod design is the kinematic coupling between the PBAs and the TS shown in Fig. 1.

The coupling mechanism can be thought of as comprising three pairs of PBAs. Each pair is connected to the TS by a "V" shaped coupling which imparts z and θ_z motion to its respective coupling point on the TS [Fig. 2(a)]. We use a 300 μm tungsten wire as the coupling, which we found to provide sufficient support for the TS whilst being flexible enough to allow PBAs to deflect. The wires are clamped at each end and set in epoxy at the tip of the V.

We find that, to the eye, the wire remains reasonably straight so that, to a first approximation, only the angle of the V changes as the PBAs deflect. Although this is not essential for the device to work, the approximation simplifies the calculation of the position of the TS, and hence, we assume that the wires remain straight when making the coordinate transformations as described below.

For each coupling point, the z and θ_z positions are controlled independently so that, with suitable coordinate transformations, the position of the TS (x, y, z, θ_x, θ_y, and θ_z) is controlled by applying the appropriate voltages to the PBAs. For example, if each piezo pair acts equally and in "self-opposition" (i.e., they bend toward or away from each other), the resulting motion of the TS is in the z direction. This happens because the coupling wires transfer the PBA motion to the z axis as the angle of the "V" changes. On the other hand, if they act equally and in "self-unison," the resultant motion of the TS is in the θ_z direction and the "V" angles remain fixed.

The transformations for movement in each of the six axes can be obtained by first defining the position P_i of each PBA as positive in the anticlockwise sense about the centre as viewed from the top [see Fig. 1(b)].

Bearing in mind that each coupling point is free to move in the direction orthogonal to the motion of its PBA pair but is constrained in the parallel direction, trigonometric considerations lead to the following transformations (to a first approximation) for motion along the principal axes.

For x motion,

$$P_1 = x, \quad P_2 = x, \quad P_3 = -x/2, \quad P_4 = -x/2, \quad P_5 = -x/2, \quad P_6 = -x/2.$$

For y motion,

$$P_1 = 0, \quad P_2 = 0, \quad P_3 = y\sqrt{3/2}, \quad P_4 = y\sqrt{3/2}, \quad P_5 = -y\sqrt{3/2}, \quad P_6 = -y\sqrt{3/2}.$$

For z motion,

$$P_1 = z, \quad P_2 = -z, \quad P_3 = z, \quad P_4 = -z, \quad P_5 = z, \quad P_6 = -z.$$

For θ_x motion,

$$P_1 = -\theta_x L/\sqrt{3}, \quad P_2 = \theta_x L/\sqrt{3}, \quad P_3 = \theta_x L/\left(2\sqrt{3}\right), \quad P_4 = -\theta_x L/\left(2\sqrt{3}\right), \quad P_5 = \theta_x L/\left(2\sqrt{3}\right), \quad P_6 = -\theta_x L/\left(2\sqrt{3}\right).$$

For θ_y motion,

$$P_1 = 0, \quad P_2 = 0, \quad P_3 = -\theta_y L/2, \quad P_4 = \theta_y L/2, \quad P_5 = \theta_y L/2, \quad P_6 = -\theta_y L/2.$$

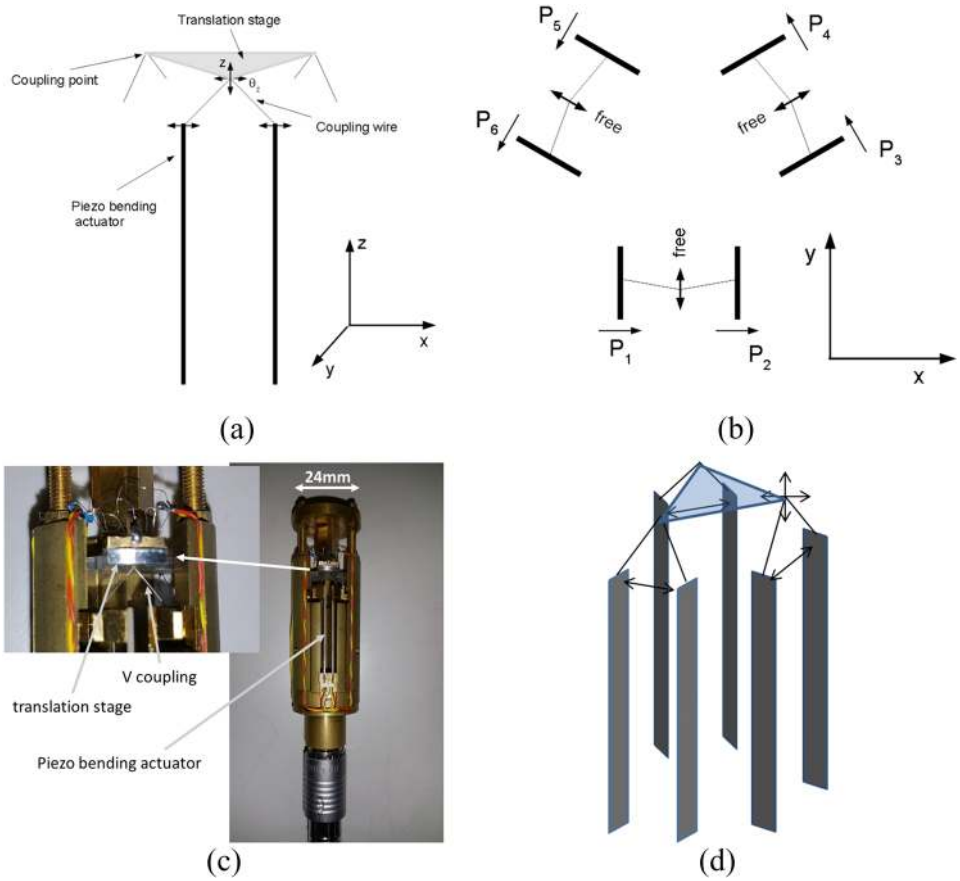

FIG. 1. Mechanical design of the Hexapod scanner. (a) Side view highlighting the operation of a single PBA pair. (b) Top view showing how the three PBA pairs are coupled to the TS, demonstrating the principle of operation of the kinematic coupling. Each coupling point is free to move in the direction orthogonal to the motion of its PBA pair but is constrained in the parallel direction. (c) Photographs of the scanner head. (d) Schematic representation of the scanner head.

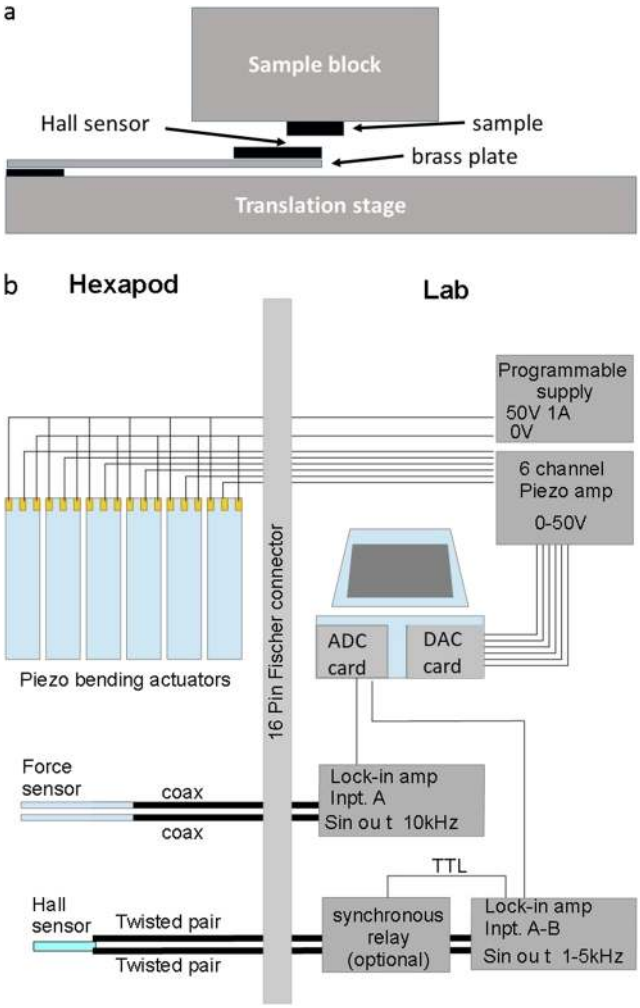

FIG. 2. (a) Diagram of the capacitive force sensor and (b) schematic representation of the electronics setup.

For θ_z motion,

$$P_1 = \theta_z L/\left(2\sqrt{3}\right),\ P_2 = \theta_z L/\left(2\sqrt{3}\right),\ P_3 = \theta_z L/\left(2\sqrt{3}\right),$$
$$P_4 = \theta_z L/\left(2\sqrt{3}\right),\ P_5 = \theta_z L/\left(2\sqrt{3}\right),\ P_6 = \theta_z L/\left(2\sqrt{3}\right),$$

where L is the distance between the coupling points. In general, the PBA coordinates P_i for a given position (x, y, z, θ_x, θ_y, and θ_z) can be found by collating the terms in the above transformations,

$$P_1 = x + z - \theta_z L/\sqrt{3} + \theta_z L/\left(2\sqrt{3}\right),$$
$$P_2 = x - z + \theta_x L/\sqrt{3} + \theta_z L/\left(2\sqrt{3}\right),$$
$$P_3 = -x/2 + y\sqrt{3/2} + z + \theta_x L/\left(2\sqrt{3}\right) - \theta_y L/2 + \theta_z L/\left(2\sqrt{3}\right),$$
$$P_4 = -x/2 + y\sqrt{3/2} - z - \theta_x L/\left(2\sqrt{3}\right) + \theta_y L/2 + \theta_z L/\left(2\sqrt{3}\right),$$
$$P_5 = -x/2 - y\sqrt{3/2} + z + \theta_x L/\left(2\sqrt{3}\right) + \theta_y L/2 + \theta_z L/\left(2\sqrt{3}\right),$$
$$P_6 = -x/2 - y\sqrt{3/2} - z - \theta_x L/\left(2\sqrt{3}\right) - \theta_y L/2 + \theta_z L/\left(2\sqrt{3}\right),$$

and each of the P_i's are set by the control voltage applied to the corresponding PBA.

B. Scan range

In our implementation, we use 4 cm long PBA's with a specified maximum travel (at room temperature) of ±500 μm. The distance between the coupling points is 11 mm. Given that, as evident from the coordinate transformations above, each of the six axes defining the TS position is thus inter-related, it is not simple to define a universal scan range for the system. For instance, the size and shape of the scan window in the x-y plane depend on Z, θ_x, θ_y, and θ_z. However, we can specify ranges under certain constraints. For example,

- At zero Z, θ_x, θ_y, and θ_z, the scan window in the X-Y plane is hexagonal with an area of ~0.7 mm^2.
- The full range in Z (i.e., with all other coordinates set zero) is 800 μm.
- The full range in each of the angular coordinates is ~4°.

For our purposes (i.e., imaging in the X-Y plane), we restrict Z, θ_x, θ_y, and θ_z to around 10% of their full range so that the range in X-Y is largely preserved. Hence, we need to mount the sample such that it is within 80 μm of the sensor and within a 2° alignment. Consequently, the sample block is mounted on three adjustable screws allowing angular (θx and θy) and Z alignment. Using an optical microscope, mounting the sample within the required alignment is relatively straightforward.

C. Capacitive sensor

Our implementation of the scanning system described above is used for scanning Hall probe (SHP) imaging. As we alluded to earlier, for SHP imaging, it is important to control the distance between the sensor and sample, or if running

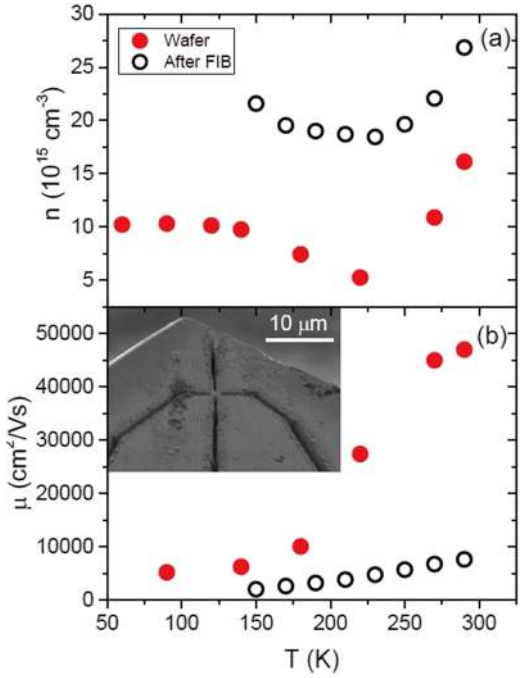

FIG. 3. Carrier concentration (a) and mobility (b) of a 900 nm InSb wafer and the Hall effect sensor after mechanical scribe and focused ion beam (FIB). Inset: a scanning electron micrograph of the FIB channels creating the Hall cross. The mechanically scribed channels are not shown.

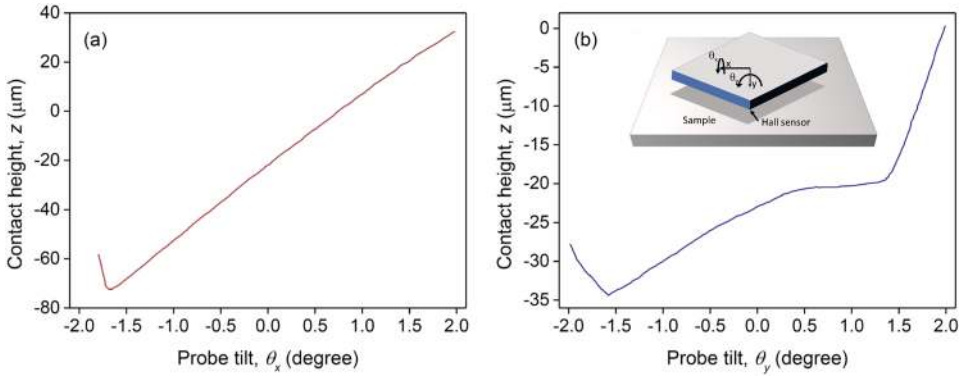

FIG. 4. Plots of the distance that the sample stage has to travel from the position z = 0 to the contact point vs. probe tilt θ_x (a) and θ_y (b). The inset in (b) shows the orientation of the axes with respect to the sample and sensor geometry.

in contact with the sample, to control the contact force. For these reasons, we mount the Hall sensor on a thin brass plate [see Fig. 2(a)], and we measure the capacitance between the plate and the TS (which is electrically isolated from the rest of the apparatus). When the sensor comes into contact with the sample, the plate deflects and the corresponding change in capacitance is detected. With this arrangement, we can determine the contact position to an accuracy of order 100 nm (corresponding to a contact force of order 10 μN). In the "contact mode," a feedback system is used to keep this deflection constant.

D. Data acquisition system

A schematic of the data acquisition system and associated electronics is shown in Fig. 2(b).

The PC controls the position of the six PBAs via an analog output board feeding into 120 V piezo amplifiers (we only operate 0-50 V). Both the signal from the Hall sensor and capacitance sensor are detected using phase sensitive detection and are recorded by monitoring the outputs of the respective lock-in amplifiers via an analog input card. This way, the software continuously measures both the Hall sensor and the capacitive force sensor while scanning the probe in X-Y fashion to build an image.

In the contact mode, a digital feedback loop is maintained by the PC software to control the contact force between the sensor and the sample and is kept as low as possible (of order 10 μN).

In the non-contact mode, the surface topology is first estimated by bringing the sensor into contact at various fixed positions in the scan window (this is usually a cross through the centre of the scan window) so as to establish a contact "plane." Mapping of the local topology would be too time consuming in most instances.

E. Synchronous relay

The synchronous relay (SR) can make significant improvements to Hall measurements (scanning measurements, in particular). First, it offers a solution to the problem of "micro-damage" to the sensor that we have found to occur when operating in the constant force mode. This results in frequent voltage jumps in the Hall probe offset as it is affected by wear (associated with microscopic damage to the sensor substrate but not the active area) and manifests itself as noise on the image [as can be seen in Fig. 5(c)]. The SR greatly reduces the electronic offset of the Hall sensor, thereby reducing the impact of micro-damage on sensor performance.

The function of the SR is to commute the current and voltage pairs half way through the AC drive cycle so that the offset is cancelled over the whole cycle (the Hall components of each half cycle add, whereas the resistive components cancel).

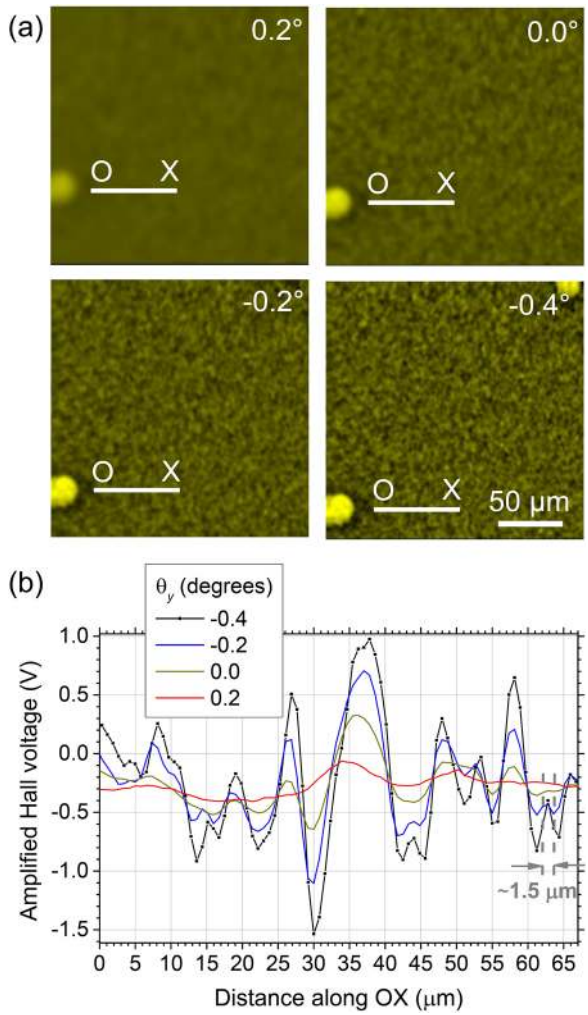

FIG. 5. A magnetic image of the thermo-magnetically patterned Nd-Fe-B film at different alignment angles θ_y. The sharpest image corresponds to $\theta_y = -0.4°$ representing the best sensor alignment. This is shown quantitatively in (b) where the line scans exhibit sharper and sharper features as the alignment position is approached, giving stronger signals and smaller feature sizes ultimately limited by the sensor active area of dimension 1.5 × 1.5 μm.

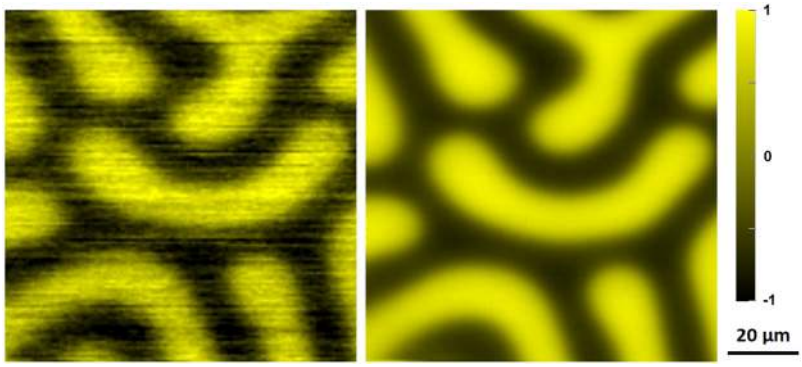

FIG. 6. Demonstration of the effect of the SR on quality of the acquired image. Left: an image of a ferrite garnet film taken without using the SR. Right: a repeat image taken using SR. The black/yellow colour scale represents the normalized output voltage of the InSb Hall sensor.

The principle is the same as in the van der Pauw measurement, only performed here synchronously with the AC drive cycle (hence the name synchronous relay). The device comprises solid state multiplexers that are triggered to switch by the transistor-transistor logic (TTL) "sync out" signal of the lock-in amplifier and are therefore phase locked to the Hall drive current. The technique works satisfactorily for frequencies up to 10 kHz.

The principle is similar to the "spinning current" approach of Ref. 29. However, in practice we find the spinning current approach to produce additional noise which we believe is due to the large resistive off-sets that are generated during the cycle. These occur because most of the time, significant current passes across the voltage pairings. By contrast, the SR switches between two Hall configurations where no such current exists.

III. RESULTS AND DISCUSSION

In order to test the performance of the scanner, we use a thermo-magnetically patterned Nd-Fe-B film (produced by Dr. Nora Dempsey at the Micro and NanoMagnetism group of Néel Institute CNRS Grenoble; see Ref. 10 for further details) as well as a commercial ferrite garnet film (provided by Dr. Mikhail Gusev, Research Institute of Materials Science and Technology, Zelenograd, Russia). The 1 μm-thick Nd—Fe—B film is patterned in circles with a 25 μm diameter that are magnetized upwards (out-of-plane), while the rest of the film is magnetized downwards. The garnet film with an out-of-plane magnetic anisotropy is characterized by a well-established maze-like domain pattern.

The sensor used was a Hall effect cross of approximate dimensions 1.5 × 1.5 μm^2 fabricated into a high mobility 900 nm thick InSb epilayer. The active area was defined in a corner of a 5 mm × 5 mm piece of wafer using a mechanical diamond scribe to define a 20 μm active area and then focus ion beam (FIB) milling to produce the fine cross features. Figure 3 shows the high mobility of the wafer (>40 000 cm^2 V^{-1} s^{-1} at room temperature). The growth recipe was developed by us previously,[30] and the unusual temperature dependence of carrier concentration and mobility was described elsewhere.[31] A significant enhancement in carrier concentration and drop in mobility are observed after FIB milling due to ion beam implantation and damage. Figure 3 also shows a scanning electron micrograph image of the sensor.

A. Sensor–sample alignment

An investigation into the effect of sensor alignment is shown in Figs. 4(a) and 4(b). In principle, at true alignment, the contact height (measured in the direction away from the sample surface) is a minimum, i.e., the sensor can be moved further toward the sample before contact is made. So as a function of θ_x and θ_y, we expect to observe a minimum in the contact height, as is shown in Fig. 4, where the minimum is defined to an accuracy of order 0.1°. The effect of alignment on the image quality is shown in Fig. 5. Inspection of the line scans in Fig. 5(b) suggests that the resulting spatial resolution of the image when the sensor is aligned is around twice that when the sensor is unaligned, while the contrast is enhanced by an order of magnitude.

B. Synchronous relay

The utility of the SR is shown in Fig. 6, where it can be seen to be very effective at eliminating apparent "noise" in the image due to micro-wear.

C. Wide area imaging

To show the spatial range of our scanning system, we have taken a magnetic image of a ferrite garnet film the in contact

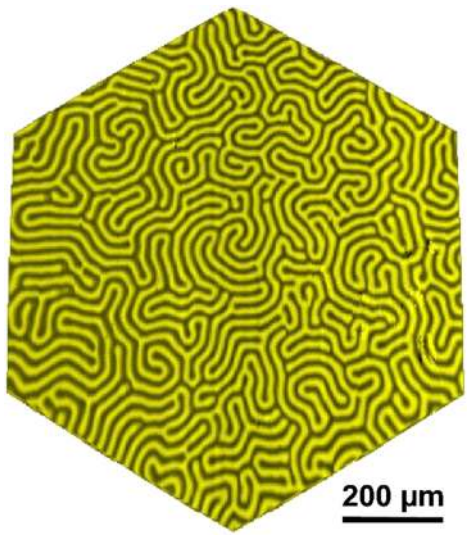

FIG. 7. Magnetic image of the domain structure in a ferrite garnet film: the whole scan range corresponding to an image area of ~0.7 mm^2.

mode over the maximum attainable spatial range (Fig. 7). Note the hexagonal nature of the image window. This is the natural boundary that results from the finite range of each of the PBAs. The slight systematic distortion visible from an ideal hexagon is due to misalignment between the sample plane and the natural scan plane which is corrected by the constant force feedback loop.

IV. CONCLUSIONS

We have described the design and functionality of a novel hexapod scanning system using piezo bending actuators. The scanning architecture could be adapted for use with a variety of sensors. We have demonstrated the utility of such a system for the purpose of scanning Hall probe imaging. In particular, the importance of alignment between the sensor and sample planes has been investigated and we have shown that the *in situ* alignment provided by our system significantly improves the image quality, in this case effectively doubling the spatial resolution and enhancing the contrast by an order of magnitude.

ACKNOWLEDGMENTS

The authors gratefully acknowledge the following individuals: Nora Dempsey, the Micro and NanoMagnetism group of Néel Institute, CNRS, Grenoble, France, for the TMP NdFeB film; Mikhail Gusev, Research Institute of Materials Science and Technology, Zelenograd, Russia, for the ferrite garnet film; and Adam Gilbertson, Imperial College London, for characterization of the InSb wafer electrical properties.

[1]A. Oral, S. J. Bending, and M. Henini, Appl. Phys. Lett. **69**, 1324 (1996).
[2]R. B. Dinner, M. R. Beasley, and K. A. Molera, Rev. Sci. Instrum. **76**, 103702 (2005).
[3]Ö. Karcı, J. O. Piatek, P. Jorba, M. Dede, H. M. Rønnow, and A. Oral, Rev. Sci. Instrum. **85**, 103703 (2014).
[4]G. Shaw, R. B. G. Kramer, N. M. Dempsey, and K. Hasselbach, Rev. Sci. Instrum. **87**(11), 113702 (2016).
[5]P. J. Curran, S. J. Bending, W. M. Desoky, A. S. Gibbs, S. L. Lee, and A. P. Mackenzie, Phys. Rev. B **89**, 144504 (2014).
[6]J. D. Moore, K. Morrison, K. A. Yates, A. D. Caplin, Y. Yeshurun, L. F. Cohen, J. M. Perkins, C. M. McGilvery, D. W. McComb, Z. A. Ren, J. Yang, W. Lu, X. L. Dong, Z. X. Zhao, Supercond. Sci. Technol. **21**(9), 092004 (2008).
[7]C.-C. Tang, H.-T. Lin, S.-L. Wu, T.-J. Chen, M. J. Wang, D. C. Ling, C. C. Chi, and J.-C. Chen, Rev. Sci. Instrum. **85**, 083707 (2014).
[8]M. Kustov, P. Laczkowski, D. Hykel, K. Hasselbach, F. Dumas-Bouchiat, D. O'Brien, P. Kauffmann, R. Grechishkin, D. Givord, G. Reyne, O. Cugat, and N. M. Dempsey, J. Appl. Phys. **108**, 063914 (2010).
[9]N. M. Dempsey, D. Le Roy, H. Marelli-Mathevon, G. Shaw, A. Dias, R. B. G. Kramer, L. V. Cuong, M. Kustov, L. F. Zanini, C. Villard, K. Hasselbach, C. Tomba, and F. Dumas-Bouchiat, Appl. Phys. Lett. **104**, 262401 (2014).
[10]F. Dumas-Bouchiat, L. F. Zanini, M. Kustov, N. M. Dempsey, R. Grechishkin, K. Hasselbach, J. C. Orlianges, C. Champeaux, A. Catherinot, and D. Givord, Appl. Phys. Lett. **96**, 102511 (2010).
[11]A. Pross, S. Bending, K. Edmonds, R. P. Campion, C. T. Foxon, and B. Gallagher, J. Appl. Phys. **95**, 3255–3227 (2004).
[12]E. Lovell, A. M. Pereira, A. D. Caplin, J. Lyubina, and L. F. Cohen, Adv. Energy Mater. **5**(6), 1401639 (2015).
[13]J. D. Moore, G. K. Perkins, Y. Bugoslavsky, M. K. Chattopadhyay, S. B. Roy, P. Chaddah, V. K. Pecharsky, K. A. Gschneidner, Jr., and L. F. Cohen, Appl. Phys. Lett. **88**(7), 072501 (2006).
[14]J. D. Moore, G. K. Perkins, Y. Bugoslavsky, L. F. Cohen, M. K. Chattopadhyay, S. B. Roy, P. Chaddah, K. A. Gschneidner, Jr., and V. K. Pecharsky, Phys. Rev. B **73**(14), 144426 (2006).
[15]J. D. Moore, K. Morrison, G. K. Perkins, D. L. Schlagel, T. A. Lograsso, K. A. Gschneidner, Jr., V. K. Pecharsky, and L. F. Cohen, Adv. Mater. **21**, 3780 (2009).
[16]K. Morrison, J. D. Moore, K. G. Sandeman, A. D. Caplin, and L. F. Cohen, Phys. Rev. B **79**, 134408 (2009).
[17]G. K. Perkins, Y. V. Bugoslavsky, X. Qi, J. L. MacManus-Driscol, and A. D. Caplin, IEEE Trans. Appl. Supercond. **11**, 3186–3189 (2001).
[18]A. Sandhu, A. Okamoto, I. Shibasaki, and A. Oral, Microelectron. Eng. **73-74**, 524 (2004).
[19]A. Sandhu, H. Masuda, K. Kurosawa, A. Oral, and S. J. Bending, Electron. Lett. **37**(1), 1335 (2001).
[20]R. Koseva, I. Mönch, J. Schumann, K.-F. Arndt, and O. G. Schmidt, Thin Solid Films **518**, 4847–4851 (2010).
[21]Z. Wang, M. Shaygan, M. Otto, D. Schalla, and D. Neumaiera, Nanoscale **8**, 7683–7687 (2016).
[22]S. Sonusen, O. Karci, M. Dede, S. Aksoy, and A. Oral, Appl. Surf. Sci. **308**, 414–418 (2014).
[23]J. Dauber, A. A. Sagade, M. Oellers, K. Watanabe, T. Taniguchi, D. Neumaier, and C. Stampfer, Appl. Phys. Lett. **106**, 193501 (2015).
[24]C.-C. Tang, M.-Y. Li, L. J. Li, C. C. Chi, and J. C. Chen, Appl. Phys. Lett. **99**, 112107 (2011).
[25]E. A. Lima, A. C. Bruno, H. R. Carvalho, and B. P. Weiss, Meas. Sci. Technol. **25**, 105401 (2014).
[26]R. G. Ballas, *Piezoelectric Multilayer Beam Bending Actuators: Static and Dynamic Behavior and Aspects of Sensor Integration*, Microtechnology and MEMS Series (Springer-Verlag, 2007), ISSN: 1615–8326; ISSN: 978-3-540-32641-1.
[27]J. Zhao, W. Gong, W. Cai, and G. Shang, Rev. Sci. Instrum. **84**, 083706 (2013).
[28]C.-L. Andrew Hung, Y.-H. Harrison Lai, T.-W. Lin, S.-G. Fu, and M. S.-C. Lu, Sens. Actuators, A **222**, 122–129 (2015).
[29]R. Steiner, Ch. Maier, A. Häberli, F.-P. Steiner, and H. Baltes, Sens. Actuators, A **66**, 167 (1998).
[30]T. Zhang, S. K. Clowes, M. Debnath, A. Bennett, C. Roberts, J. J. Harris, R. A. Stradling, and L. F. Cohen, Appl. Phys. Lett. **84**, 4463–4465 (2004).
[31]J. J. Harris, T. Zhang, W. R. Branford, S. K. Clowes, M. Debnath, A. Bennett, C. Roberts, and L. F. Cohen, Semicond. Sci. Technol. **19**(12), 1406–1410 (2004).